The effect of cubic stiffness nonlinearity on the vortex-induced vibration of a circular cylinder at low Reynolds numbers

Enhao Wang[a], Wanhai Xu[a,*], Xifeng Gao[a], Liqin Liu[a], Qing Xiao[b], Kiran Ramesh[c]

[a]*State Key Laboratory of Hydraulic Engineering Simulation and Safety, Tianjin University, Tianjin 300072, China*
[b]*Department of Naval Architecture, Ocean and Marine Engineering, University of Strathclyde, Glasgow G4 0LZ, UK*
[c]*Aerospace Sciences Division, School of Engineering, University of Glasgow, Glasgow G12 8QQ, UK*

Abstract

The vortex-induced vibration (VIV) of a circular cylinder elastically supported by linear and cubic springs is investigated numerically at low Reynolds numbers. The cylinder has a low mass ratio and zero structural damping. Nine dimensionless cubic stiffness nonlinearity strength values are considered. It is found that within the parameter space examined, the VIV response for the linear and softening springs can be divided into four regimes, namely the initial, upper, lower and desynchronised regimes. When the softening spring nonlinearity gets stronger, there exist a reduction in the peak amplitude and shifts in the initial-upper branch and upper-lower branch transitions to lower Reynolds number ranges. In contrast, as the hardening spring nonlinearity increases, the response envelope moves to a higher Reynolds number range and the profile of the initial and upper branches becomes smoother with the lower branch gradually disappearing. In the hardening spring case, the beating response is observed near the low end of the initial branch up to the high end of the initial branch. The modulations in the vibration amplitude gradually diminish with increasing Reynolds number. The cubic spring results coincide with those of the linear spring when they are presented with the equivalent reduced velocity. Due to the low Reynolds number range considered, the majority of the vortex shedding is in the 2S mode. The wake in the cases with smaller vibration amplitudes exhibits a single-row configuration.

*Corresponding author
Email address: xuwanhai@tju.edu.cn (Wanhai Xu)

Whereas, a double-row vortex street is mainly observed in the upper branch. Disorders in the wake are found to be associated with beating responses which have larger vibration amplitudes.

Keywords: Cubic stiffness nonlinearity, Vortex-induced vibration (VIV), Low Reynolds numbers, Fluid-structure interaction (FSI)

1. Introduction

Vortex-induced vibration (VIV) is a fluid-structure interaction (FSI) phenomenon in which the structure is excited into vibration under the forces induced by the vortices alternatively shed from the surfaces of a bluff body, e.g., a circular cylinder. VIV is a main factor which has the potential to cause the fatigue failure of the structures in many engineering applications and its practical importance has led to the recent advancement in the fundamental studies on this subject. One may refer to the famous books and review articles by Blevins (1986), Williamson and Govardhan (2004), Gabbai and Benaroya (2005), Sumer and Fredsøe (2006), Bearman (2011) and Païdoussis et al. (2014). The VIV response of a circular cylinder in uniform flow is characterised by the Reynolds number, the mass ratio, the damping ratio and the reduced velocity. The Reynolds number is defined as $Re = U_\infty D/\nu$, where U_∞ is the freestream velocity, D is the cylinder diameter and ν is the kinematic viscosity of the fluid. The mass ratio is defined as $m^* = 4m/\rho\pi D^2$ with m and ρ being the mass per unit length and the fluid density, respectively. The damping ratio is the ratio of the structural damping coefficient to the critical damping, i.e., $\zeta = c/c_{crit} = c/2\sqrt{km}$, where k is the linear spring stiffness. The reduced velocity which can be viewed as a ratio of the wavelength of the cylinder trajectory to its diameter (Blevins, 1986; Sumer and Fredsøe, 2006) is given by $V_r = U_\infty/f_n D$, in which f_n is the structural natural frequency of the linear system.

The majority of the previous studies have been focused on the one-degree-of-freedom (1DOF) cross-flow VIV of a circular cylinder. When a cylinder is subject to the VIV, the lock-in phenomenon of the cylinder response occurs in a range of the reduced velocities (Bourguet et al., 2011; Zhao, 2015). For high m^*, Bearman (1984) discussed in his review that the transverse oscillation frequency of the cylinder (f_y) in the lock-in range was close to the vortex shedding frequency (f_v) and also close to f_n resulting in $f_y/f_n \approx 1$. Similar frequency responses were observed by Feng (1968) and Brika and Laneville (1993) in their experimental tests. At high mass-damping parameter ($m^*\zeta$), there existed two different response branches, i.e., the initial branch and the lower branch (Khalak and Williamson, 1999; Govardhan and Williamson,

2000). The corresponding vortex shedding patterns were the 2S mode (two single vortices are shed from the cylinder in one cycle of vibration) in the initial branch and the 2P mode (two pairs of vortices are shed from the cylinder in one cycle of vibration) in the lower branch, respectively. If $m^*\zeta$ is low, a further large-amplitude upper branch of response appeared with the associated wake mode being the 2P mode (Govardhan and Williamson, 2000). The research by Khalak and Williamson (1997) on the VIV of an elastically mounted rigid cylinder with low $m^*\zeta$ showed that unlike the classical lock-in for the high $m^*\zeta$ cases where f_y matched f_n, f_y of a low $m^*\zeta$ system deviated from the natural frequency through the excitation range.

Many numerical studies on the 1DOF VIV of a circular cylinder were performed at low Re using two-dimensional (2D) numerical models. Blackburn and Henderson (1996) presented results for 2D numerical simulations of the cross-flow VIV of a circular cylinder at $Re = 250$. The lock-in phenomenon was observed in their numerical simulations and chaotic responses were found over a range of the cylinder natural frequencies. The branching behaviour of the VIV of a circular cylinder free to vibrate in the transverse direction at $Re = 200$ was numerically investigated by Leontini et al. (2006). Two synchronous response branches which resemble the upper and lower branches in the higher Re experiments were found to exist when the cylinder was subject to the VIV. They also suggested that the branching behaviour at higher Re was not caused by the presence of the three-dimensionality. Ahn and Kallinderis (2006) and Placzek et al. (2009) simulated the 1DOF VIV of a circular cylinder at $Re = 150$ and $Re = 100$, respectively. The numerical results showed very good agreement with other computational and experimental results. The 1DOF VIV of an elastically mounted circular cylinder has also been studied numerically at higher Re in the subcritical regime. Guilmineau and Queutey (2004) and Pan et al. (2007) performed numerical simulations of the 1DOF VIV of a circular cylinder in the cross-flow direction by employing 2D Reynolds-Averaged Navier-Stokes (RANS) codes with the shear stress transport (SST) $k - \omega$ turbulence model. Both studies were able to reproduce the initial and lower branches, but their results showed obvious discrepancies in the upper branch in comparison with the measured data in the experiments.

It should be noted that the FSI systems in all the aforementioned studies involved a circular cylinder elastically supported by a linear spring and the structural force was provided by a simple spring-damper system, i.e., $F_{struct} = -b\dot{y} - ky$, where b is the structural damping coefficient, y is the cylinder displacement in the cross-flow direction and a dot denotes differentiation with respect to time. However, recent studies on mechanical and fluid-structure systems with nonlinearities in the restoring forces have re-

vealed that the nonlinear restoring forces can either increase the vibration amplitudes and enhance the ranges of stable oscillations with potential applications in vibration energy harnessing (Barton et al., 2010; Gammaitoni et al., 2009; Ramesh et al., 2015; Wang et al., 2018) or decrease the vibration amplitudes viable for vibration suppression (Bert et al., 1990; Lee et al., 2008; Gendelman et al., 2010). Research into the VIV of a circular cylinder supported by nonlinear springs is still quite limited. Stappenbelt (2010) studied the one- and two-degree-of-freedom VIV of a nonlinearly compliant elastically mounted rigid circular cylinder. In the parameter space they considered, the nonlinear compliance had an effect of decreasing the VIV response amplitudes. The intial lock-in point appeared to remain unchanged with the nonlinear compliance and when the linear system still-water natural frequency was used in the normalisation of the flow velocity, evident shifts in the amplitude, frequency and drag force responses along V_r were observed. The VIV amplitudes of a circular cylinder supported by linear and various nonlinear springs were experimentally examined by Mackowski and Williamson (2013). They found that one might understand and predict the response of a nonlinear structural system using the knowledge of a standard linear VIV system. Moreover, a VIV-based energy harnessing device could operate at high performance over a much larger range of Re than a standard system by applying appropriate spring nonlinearities. Ma et al. (2016) investigated the hydrokinetic power conversion using the flow-induced vibration of a single, rigid circular cylinder with passive turbulence control (PTC) and piecewise continuous restoring forces. It was found that the lowest flow velocity at which the nonlinear piecewise spring converter could harness energy was 0.275 m/s and the nonlinear spring converter had up to 76% better performance than its linear counterpart. Sun et al. (2018) conducted experiments to study the hydrokinetic power conversion of a nonlinear circular cylinder oscillator with PTC using a cubic-spring restoring function. Their results showed that the cubic stiffness function was an effective way to increase the power conversion efficiency over a wide range of the flow velocities. In the upper and lower VIV branches, the harnessed power increased with increasing nonlinearity and a 100% increase in the harnessed power was observed for a strongly nonlinear system. In the flow velocity range corresponding to the galloping, at low harness damping, the increase in the oscillation amplitude resulted in higher natural frequency of the oscillator in water and thus enhanced the harnessed power. Whereas at high harness damping, the harnessed power increased regardless of the natural frequency of the oscillator in water.

It can be seen from the literature review, there is a lack of comprehensive studies on the VIV with nonlinear restoring forces. Therefore, in the present

study, 2D numerical simulations of the cross-flow VIV of a circular cylinder elastically mounted by linear and cubic springs are conducted at low Re in an effort to evaluate the effect of the cubic stiffness nonlinearity on the important aspects of the VIV, such as the amplitude response, the frequency response, the hydrodynamic coefficients and the vortex shedding modes. The rest of the paper is arranged as follows. The numerical methods adopted in this study are given in Section 2 and a description of the problem investigated in the present research is provided in Section 3. In Section 4, the results are presented and analysed in detail. Finally, this paper is concluded in Section 5.

2. Numerical methods

2.1. Flow model

The flow around the cylinder is modelled by solving the 2D incompressible Navier-Stokes equations. An arbitrary Lagrangian-Eulerian (ALE) scheme is applied to deal with the moving boundary of the circular cylinder. The governing equations in ALE formulation are outlined as follows.

$$\frac{\partial u_i}{\partial x_i} = 0, \tag{1}$$

$$\frac{\partial u_i}{\partial t} + (u_j - \hat{u}_j)\frac{\partial u_i}{\partial x_j} = -\frac{1}{\rho}\frac{\partial p}{\partial x_i} + \nu\frac{\partial^2 u_i}{\partial x_j \partial x_j}, \tag{2}$$

where x_i represents the Cartesian coordinate, u_i and $\hat{u}_i$ respectively are the fluid velocity component and the grid velocity component in the x_i-direction, t denotes the time and p stands for the pressure.

The open source computational fluid dynamics (CFD) toolbox OpenFOAM (OpenFOAM, 2015) is utilised to simulate the flow field. The Navier-Stokes equations are discretised with a finite volume method (FVM). A second-order implicit backward Euler scheme is employed to discretise the transient term, while second-order Gaussian integration schemes are used for the gradient, divergence and Laplacian terms. The pressure-implicit with splitting of operators (PISO) algorithm introduced by Issa (1986) is adopted to solve the continuity and momentum equations together in a segregated manner.

2.2. Structural dynamic model

The dynamics of a 1DOF VIV system with cubic stiffness nonlinearity can be described by

$$m\ddot{y} + b\dot{y} + ky + cy^3 = F_y, \tag{3}$$

where c is the dimensional strength of the cubic stiffness nonlinearity and F_y is the hydrodynamic force in the transverse direction.

The implicit Newmark-beta method with second-order accuracy as detailed in Newmark (1959) is used to integrate the equation of motion. This method relates the displacement, velocity and acceleration from time step n to $n+1$ in the following way:

$$\dot{y}^{n+1} = \dot{y}^n + \Delta t[(1-\gamma)\ddot{y}^n + \gamma\ddot{y}^{n+1}], \tag{4}$$

$$y^{n+1} = y^n + \Delta t\dot{y}^n + \frac{\Delta t^2}{2}[(1-2\beta)\ddot{y}^n + 2\beta\ddot{y}^{n+1}], \tag{5}$$

herein the superscripts represent the time-step numbers. Δt is the time-step size. β and γ are two real parameters directly linked to the accuracy and stability of the integration method. In this study, $\beta = 1/4$ and $\gamma = 1/2$ are chosen corresponding to a trapezoidal rule with unconditional stability.

2.3. Fluid-structure interaction

The FSI in the present study is based on a loosely coupled approach, i.e., the flow field and the dynamic response of the structure are solved successively at a given time step (Placzek et al., 2009). Here, we briefly describe the FSI procedures within one time step: (i) the flow equations are solved to obtain the hydrodynamic loads on the circular cylinder; (ii) the computed hydrodynamic loads are applied to the structural dynamic solver to yield the motion quantities of the circular cylinder; (iii) spherical linear interpolation (SLERP) of the motion quantities as a function of the distance to the cylinder surface is performed to compute the new mesh field (including the new mesh positions and the mesh velocities); (iv) the velocity boundary conditions corresponding to the moving cylinder are updated and (v) the next time step begins by solving the Navier-Stokes equations on the updated mesh.

3. Description of the problem

3.1. Simulation parameters

In this study, 2D numerical simulations are conducted for an elastically mounted circular cylinder with a diameter of $D = 0.01$ m and a mass ratio of $m^* = 2.546$. The circular cylinder is only allowed to vibrate in the cross-flow direction. A low Re range of $60 \leq Re \leq 200$ is adopted in the present simulations. The selection of this Re range stems from the following important considerations. It is well known that the vortex shedding phenomenon is observed for a circular cylinder as Re exceeds 40. That the lowest Re takes the value of 60 guarantees the occurrence of the vortex shedding and

the consequent VIV in the Re range we consider. The wake flow behind a stationary cylinder becomes three-dimensional (3D) if Re is greater than 170 – 200 (Williamson, 1988) and the Re range of $200 \leq Re \leq 400$ is found to be the transitional regime, where the flow transits from 2D laminar flow to 3D turbulent flow (Bloor, 1964; Williamson, 1988). The upper bound of the Reynolds number $Re = 220$ in the present research is slightly higher than the lower bound of the transitional regime for stationary circular cylinder wake. However, Leontini et al. (2007) demonstrated that the wake of a transversely oscillating cylinder in a uniform cross flow could effectively remain 2D for $Re \leq 280$ as a result of the increased correlation length of the flow vortical structures in the spanwise direction due to the oscillations of the cylinder. Therefore, the flow is essentially 2D in the range of Re considered in this study, which can be modelled by directly solving the 2D unsteady incompressible Navier-Stokes equations without the potential uncertainties introduced by the utilisation of turbulence models. More importantly, previous studies by Bao et al. (2012), Leontini et al. (2006) and Wang et al. (2017) revealed that the VIV of rigid structures at low Re share comparable response features to that at high Re. Furthermore, studies on the VIV at low Re are also of fundamental research interest from a flow physics point of view. The linear spring stiffness is fixed at $k = 0.39$ N/m. As a result of the difference in Re, the maximum amplitudes obtained from the numerical computations of the VIV at low Re are significantly lower than the peak responses found in the experiments with typical values of $Re = 10^3 - 10^5$ (Khalak and Williamson, 1997, 1999). Therefore, in order to maximise the vortex-induced response of the cylinder, the damping coefficient is set to zero (i.e., $b = 0$) in the present simulations.

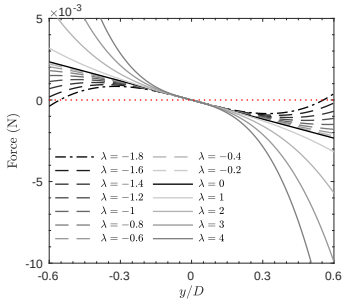

Fig. 1. Restoring force nonlinearity on VIV.

In essence, the structure considered in this study is a Duffing oscillator. When the value of c is positive, the restoring force increases disproportionately as the spring is stretched. This type of nonlinearity is known as a hardening spring. On the contrary, for a negative value of c, the restoring

force ultimately decreases with the stretching spring, which is referred to as a softening spring. The dimensionless measure λ introduced by Mackowski and Williamson (2013) is used to quantify the strength of the nonlinearity. The normalised nonlinearity strength can be expressed as $\lambda = D/\sqrt{k/c}$ and $\lambda = -D/\sqrt{-k/c}$ for hardening and softening springs, respectively. Fig. 1 demonstrates how the restoring force varies with the nondimensional displacement for different λ values. Previous numerical results by Ahn and Kallinderis (2006) and Borazjani and Sotiropoulos (2009) suggested that the maximum attainable amplitude of the 1DOF VIV of an elastically mounted circular cylinder with $m^* = 2.546$ and $b = 0$ in similar low Re ranges was smaller than $0.6D$. Hence, the nondimensional displacement range used to determine the nonlinearity of the restoring force in Fig. 1 is restricted to $-0.6 \leq y/D \leq 0.6$. According to Mackowski and Williamson (2013), λ cannot be decreased infinitely. For a softening spring, as its λ is decreased, eventually it will reach a point at which the sign of the restoring force flips leading to instability. As shown in Fig. 1, in the current parameter space, flips in the sign of the restoring force are observed at $\lambda = -1.8$ indicating that the nonlinear VIV system is unstable when λ is reduced to -1.8. In order to avoid the instability of the system and the associated divergent oscillations which may occur, the lowest λ value considered in the present simulations is $\lambda = -1.6$. Then, nine values of λ ranging from -1.6 to 4 are selected for investigation including $\lambda = 0$, which is equivalent to a linear VIV system.

3.2. Computational domain and boundary conditions

Fig. 2(a) demonstrates the computational domain which is used in the present study. The size of the domain is $30D \times 20D$. The centre of gravity (COG) of the cylinder is located at $10D$ downstream the inlet boundary along the longitudinal centreline of the domain. The boundary conditions for the governing equations are as follows. The surface of the cylinder is assumed to be smooth on which a no-slip boundary condition ($u = 0$ and $v = \dot{y}$) is imposed. A Dirichlet boundary condition is applied to the inlet boundary as $u = U_\infty$ and $v = 0$, while the gradients of the fluid velocity in the streamwise direction are set to zero on the outlet boundary. A free-slip boundary condition with the velocity in the direction normal to the boundary being zero is used on the two transverse boundaries. A zero gradient boundary condition is adopted for the pressure on all the boundaries except the outlet boundary where a zero reference pressure ($p_{ref} = 0$) is employed. The initial conditions for the motion quantities of the cylinder are assigned as $y = 0$ and $\dot{y} = 0$. Similar computational domain size and boundary conditions have been used in our previous numerical simulations of the VIV of rigid and flexible cylinders (Wang and Xiao, 2016; Wang et al., 2017).

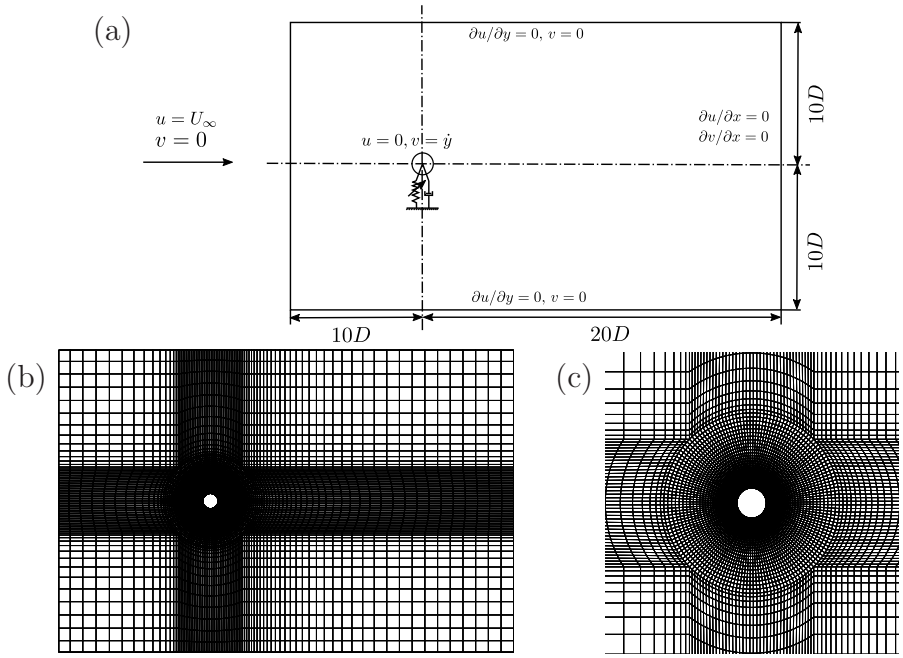

Fig. 2. (a) Computational domain, (b) computational mesh and (c) close-up of the mesh around the cylinder.

3.3. Validation test

The validation case is the transverse-only VIV of a circular cylinder with a mass ratio of $m^* = 2.546$ and zero structural damping at a fixed Re of 150. Fig. 3(a) shows the comparison of the calculated nondimensional response amplitude (A_y/D) with the numerical results by Bao et al. (2012) and Zhao (2013). The variations of A_y/D with V_r from the different models are similar to each other. The hydrodynamic forces are computed by summing the dot products of the pressure and viscous forces with the specified force vector over the cylinder surface. The drag and lift force coefficients are defined as $C_D = 2F_x/\rho U_\infty^2 D$ and $C_L = 2F_y/\rho U_\infty^2 D$, respectively. The comparison of the mean drag coefficient ($\overline{C}_D$), the root mean square drag coefficient (C'_D) and the root mean square lift coefficient (C'_L) between the present simulations and those by Zhao (2013) is presented in Fig. 3(b). The agreement between the two sets of results is very good. This test case demonstrates that the present numerical methods are capable of accurately capturing the VIV response of an elastically mounted circular cylinder at low Re.

3.4. Mesh dependency study and time-step size selection

In order to examine the dependency of the numerical results on the mesh density, numerical simulations are performed for the linear spring scenario

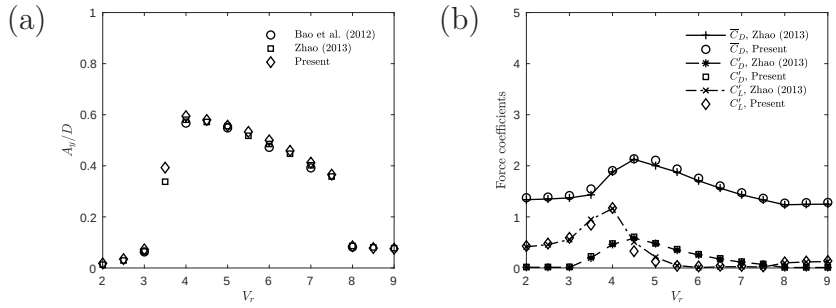

Fig. 3. Comparison of (a) the response amplitude and (b) the hydrodynamic force coefficients against the reduced velocity for the 1DOF VIV of a circular cylinder with available numerical results: $m^* = 2.546$ and $Re = 150$.

in this study (i.e., $\lambda = 0$) at $Re = 100$. The mesh generation parameters together with the numerical results are tabulated in Table 1 where N_{node}, $N_{element}$, N_c and Δr are the number of nodes, the number of elements, the number of nodes along the circumference of the cylinder and the minimum mesh size next to the cylinder surface in the radial direction, respectively. The results (A_y/D, $\overline{C}_D$, C'_D and C'_L) from three different mesh systems are compared. It can be seen that the maximum percentage difference between Mesh 1 and Mesh 2 is 3.68% observed for C'_L, whereas it is reduced to 1.6% with the further refinement of the computational mesh from Mesh 2 to Mesh 3. Therefore, balancing the accuracy and the computational efforts, Mesh 2 which consists of a total of 10692 nodes and 10929 elements is used in the numerical simulations in this paper. The computational mesh and a close-up of the mesh around the cylinder are presented in Figs. 2(b) and (c), respectively.

Table 1 Comparison of the results from three different meshes.

Mesh	N_{node}	$N_{element}$	N_c	$\Delta r/D$	A_y/D	$\overline{C}_D$	C'_D	C'_L
1	6306	6489	120	0.02	0.587	2.416	0.578	0.572
2	10692	10929	160	0.01	0.592	2.393	0.581	0.593
3	33924	34320	240	0.005	0.593	2.381	0.578	0.603

The Courant-Friedrichs-Lewy (CFL) condition ($C_o \leq C_{o\max}$, where C_o is the Courant number and $C_{o\max}$ is the maximum Courant number) is a necessary condition for convergence while solving the Navier-Stokes equations numerically. The principle behind this condition is that if the flow is moving across a discrete spatial grid and its characteristics are supposed to be computed at discrete time steps of equal duration, then this duration (i.e., the time-step size Δt) must be equal to or less than the time it takes for

a fluid particle to move from one cell to the next. The detailed values of $C_{o\max}$ depend on the particular scheme. In order to accurately resolve the transient details in the present numerical simulations, Δt is selected in such a way that the corresponding C_o is less than 0.5.

4. Results and Discussion

The 1DOF VIV of a circular cylinder elastically supported by linear and cubic springs is numerically simulated in a Re range of $Re = 60 - 220$. Nine different dimensionless nonlinearity strength values are considered (i.e., $\lambda = -1.6, -1.2, -0.8 - 0.4, 0, 1, 2, 3$ and 4). The effect of the cubic stiffness nonlinearity on the cross-flow VIV response characteristics and the flow features around the vibrating cylinder is investigated.

4.1. Amplitude response and response regimes

The variation of A_y/D of a circular cylinder restrained by a cubic spring with Re is demonstrated in Fig. 4. The results of the linear spring case ($\lambda = 0$) are included in both Figs. 4(a) and (b) for comparison. V_r is a commonly used scaling in the VIV studies to present the response data. According to the definition provided in Section 1, f_n of the system needs to be known in order to calculate V_r. However, the natural frequency of a cubic spring is a function of the vibration amplitude rather than a constant as it is in the linear spring case, which makes the standard form of V_r not applicable to the nonlinear VIV. Therefore, the results are presented with respect to Re rather than V_r in the first place.

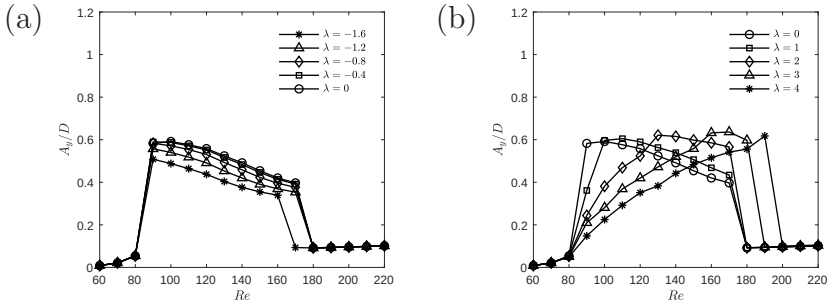

Fig. 4. Variation of the response amplitude with the Reynolds number: (a) $\lambda \leq 0$ and (b) $\lambda \geq 0$.

It can be seen from Fig. 4(a) that similar to the numerical results by Leontini et al. (2006) at $Re = 200$, the synchronous regions with larger amplitudes in the softening spring cases demonstrate continuously decreasing trends. The A_y/D curve of $\lambda = -0.4$ coincides with that of $\lambda = 0$. Their lock-in

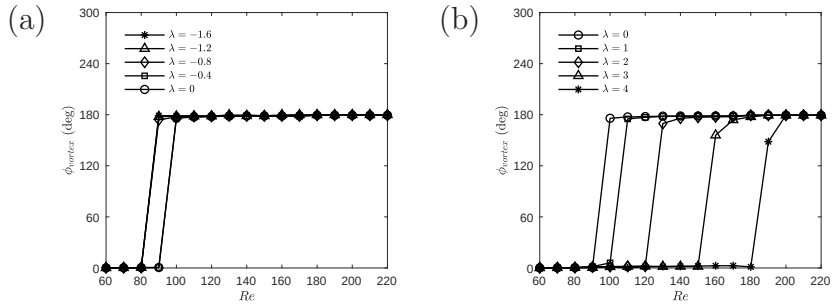

Fig. 5. Vortex phase as a function of the Reynolds number: (a) $\lambda \leq 0$ and (b) $\lambda \geq 0$.

ranges are $Re = 90 - 170$. The maximum A_y/D values around 0.6 of the two curves are both observed at $Re = 100$. These observations indicate that at the low Re range considered in the present study, $\lambda = -0.4$ has a negligible effect on the amplitude response of the cylinder. As the softening spring nonlinearity becomes stronger (i.e., λ is decreased), the A_y/D curves of $\lambda = -0.8$ and -1.2 get lower than those of $\lambda = 0$ and -0.4 with the maximum A_y/D values appearing at $Re = 90$. The synchronous regions remain unchanged in the range of $Re = 90 - 170$. With a further decrease in λ to the lowest value considered in the present study ($\lambda = -1.6$), the corresponding A_y/D curve becomes even lower and the maximum A_y/D at $Re = 90$ decreases to 0.51. The larger-amplitude region shrinks to $Re = 90 - 160$.

Govardhan and Williamson (2000) argued that the transition between the initial and upper branches involved a jump in the vortex phase ϕ_{vortex} which is the phase between the vortex force and the displacement. In order to examine how the cubic stiffness nonlinearity affects the initial-upper branch transition, ϕ_{vortex} is plotted as a function of Re for different λ values in Fig. 5. Here, ϕ_{vortex} is taken as the time average of the instantaneous vortex phase which is computed with the use of the Hilbert transform (see Khalak and Williamson (1997) for details). As shown in Fig. 5(a), the transitional regions between the initial and upper branches of $\lambda = 0$ and -0.4 are identical with the range of $Re = 90 - 100$. When λ is decreased, the initial-upper branch transition in the cases of $\lambda = -0.8, -1.2$ and -1.6 occurs at a lower Re range of 80 – 90. The second mode transition for a low mass-damping VIV system is associated with a jump in the total phase, ϕ_{total} which is the phase between the lift force and the displacement (Govardhan and Williamson, 2000). Fig. 6 depicts ϕ_{total} against Re for different λ values. Similar to ϕ_{vortex}, ϕ_{total} is represented by the mean value of the instantaneous total phase determined with the Hilbert transform. It can be observed from Fig. 6(a) that the variation of ϕ_{total} with Re for $\lambda = -0.4$ shares a similar trend to that for $\lambda = 0$. ϕ_{total} is

approximately 0° at the start of the upper branch ($Re = 100$). As Re is gradually increased, ϕ_{total} progressively climbs to about 170° in the range of $Re = 110 - 140$. This process denotes that the response of the cylinder transits from the upper branch to the lower branch. The transition region between upper and lower branches moves towards a lower Re range with decreasing λ. At the lowest λ value considered in this study, the Re range corresponding to the upper-lower branch transition shifts to $Re = 90 - 110$. ϕ_{vortex} and ϕ_{total} are 0° in the initial branch and 180° in the desynchronised region, respectively.

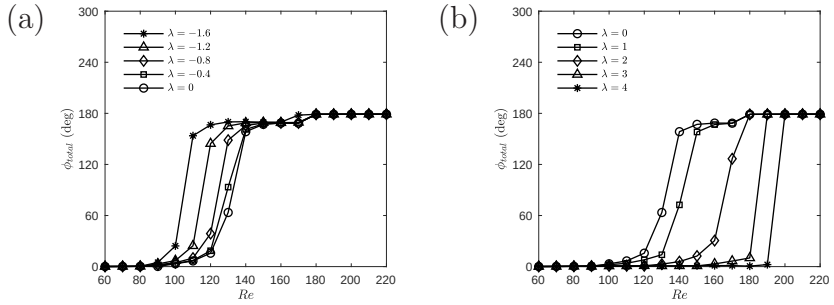

Fig. 6. Total phase versus the Reynolds number: (a) $\lambda \leq 0$ and (b) $\lambda \geq 0$.

Compared to the softening spring, the effect of the hardening spring on the cylinder response is more pronounced. It can be observed from Fig. 4(b), as λ is increased, the amplitude response envelope shifts to a higher Re range and the response amplitude undergoes a smoother variation to its maximum value, which is similar to the observations of Stappenbelt (2010) and Mackowski and Williamson (2013) in the subcritical Re regimes. This is particularly beneficial for energy extraction from the VIV as it indicates that employing a proper hardening spring is an effective way to maintain the energy harnessing efficiency over a wider range of the flow velocities (Sun et al., 2018). The maximum A_y/D experiences an increase from 0.6 to 0.64 when λ is increased from 0 to 3. Whereas a slight decrease in the maximum A_y/D to 0.62 is observed as λ is further increased to the highest values considered in the present simulations, $\lambda = 4$. Nevertheless, the effect of the hardening spring nonlinearity on the maximum attainable amplitude is subtle compared to the influence of the softening spring nonlinearity.

Fig. 5(b) reveals that as the hardening spring nonlinearity grows stronger, the jump in ϕ_{vortex} corresponding to the transition from the initial branch to the upper branch is delayed from $Re = 100 - 110$ for $\lambda = 1$ to $Re = 180 - 190$ for $\lambda = 4$. The jump in ϕ_{total} also shifts to a higher Re range from $Re = 120 - 140$ to $Re = 190 - 200$ when λ is increased from 1 to 4. In the

meanwhile, ϕ_{total} undergoes a steeper variation with Re as λ is increased, which reflects that the lower branch gradually diminishes with increasing λ. When $\lambda = 3$ and 4, the VIV response of the cylinder switches directly from the upper branch to the desynchronised branch. An amplitude response distinctly different from that of the linear system has also been reported by Mackowski and Williamson (2013) for high hardening spring nonlinearity strength.

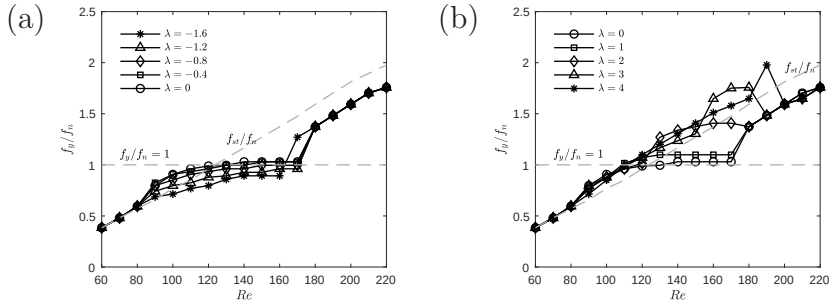

Fig. 7. Response frequency against the Reynolds number: (a) $\lambda \leq 0$ and (b) $\lambda \geq 0$.

4.2. Frequency response and response characteristics

The variation of the nondimensional response frequency (f_y/f_n) with Re is presented in Fig. 7, where f_y is the primary frequency of the response defined as the frequency with the highest power content from the power spectral density (PSD) of the response and f_n is the natural frequency of the linear VIV system given by

$$f_n = \frac{1}{2\pi}\sqrt{\frac{k}{m}}. \tag{6}$$

As illustrated in Fig. 7(a), the f_y/f_n curves of $\lambda = 0, -0.4$ and -0.8 are nearly identical. In the initial excitation range ($60 \leq Re \leq 80$), f_y/f_n follows the Strouhal frequency (f_{st}/f_n) which varies almost linearly with Re. In the range of $Re = 90 - 110$, f_y/f_n departs from f_{st}/f_n with its value consistently lower than $f_y/f_n \approx 1$ whereas f_y synchronises with f_n when $120 \leq Re \leq 170$. This step change in the response frequency is associated with the transition from the upper branch to the lower branch as discussed by Khalak and Williamson (1999) and Leontini et al. (2006). In the desynchronised region, f_y/f_n returns to a linear function of Re. The overall frequency responses of those three λ values agree with the previous numerical results by Zhao et al. (2014) and Wang et al. (2017) for the VIV of a linear system. For the two cases with stronger softening springs (i.e., $\lambda = -1.2$ and -1.6), the

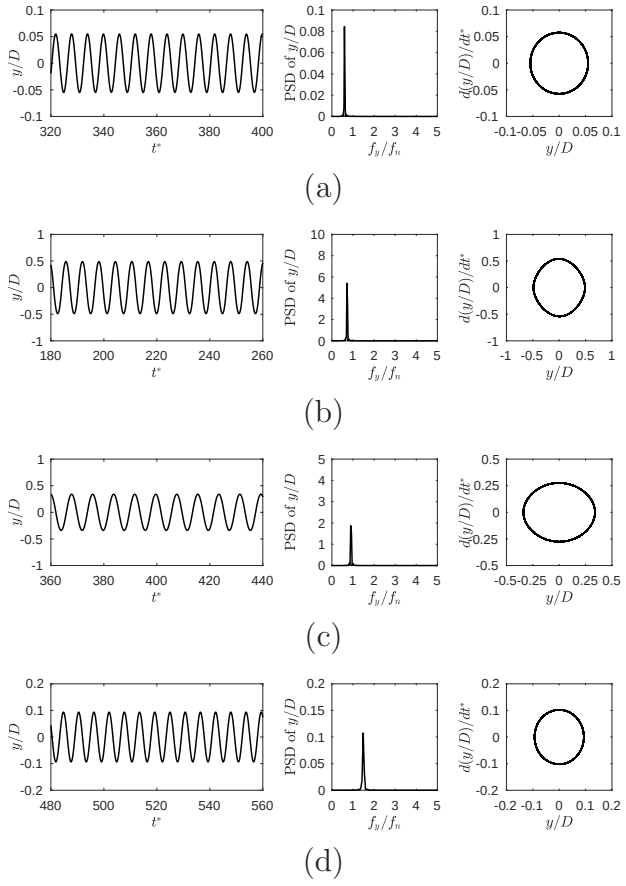

Fig. 8. Time history, power spectral density and phase-plane plots in different response regimes for $\lambda = -1.6$: (a) $Re = 80$, (b) $Re = 100$, (c) $Re = 160$ and (d) $Re = 190$.

f_y/f_n curves coincide with the other three curves in the initial excitation and desynchronised regions but deviate from the f_y/f_n curves for $\lambda = 0, -0.4$ and -0.8 in the synchronous region with f_y/f_n slightly lower than 1. In particular, the frequency synchronisation of $\lambda = -1.6$ ends at $Re = 160$ which is earlier than $Re = 170$ in the other four cases. This observation agrees with the discussions about the synchronous range based on Fig. 4(a).

When $\lambda > 0$, the frequency response behaviours in the initial excitation range and the desynchronised range are in agreement with that for $\lambda = 0$. For a moderate λ value ($\lambda = 1$), the variation trend of f_y/f_n with Re is analogous to that of the linear system with f_y/f_n in the frequency synchronisation region for $\lambda = 1$ being a bit higher than $f_y/f_n \approx 1$ in the linear spring case. With the increase in λ, the frequency response departs from the linear spring frequency response and exhibits nonlinear variation with Re. As mentioned in Section 4.1, the natural frequency of a cubic spring depends on the vibra-

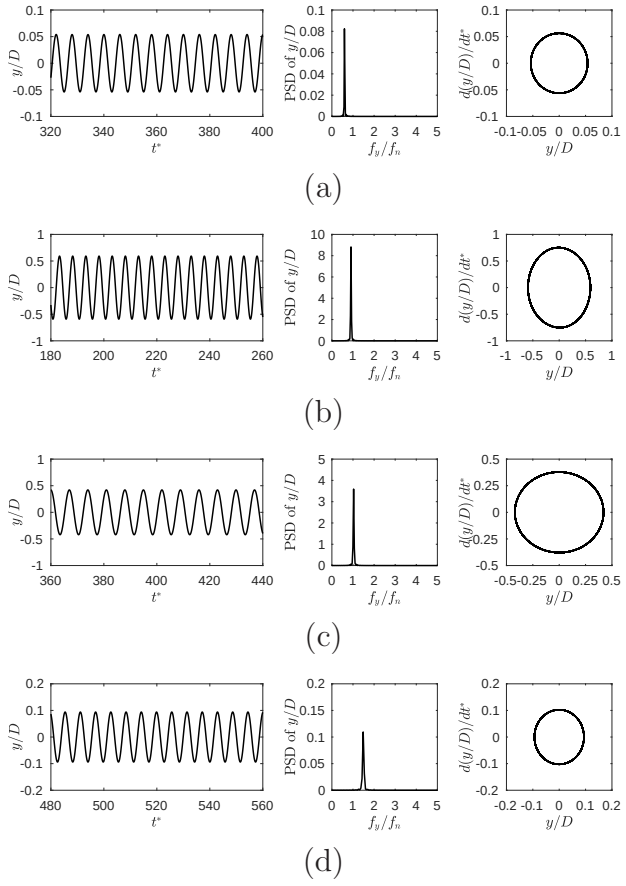

Fig. 9. Time history, power spectral density and phase-plane plots in different response regimes for $\lambda = 0$: (a) $Re = 80$, (b) $Re = 100$, (c) $Re = 160$ and (d) $Re = 190$.

tion amplitude. When f_y is normalised with respect to the constant f_n of the linear system in Fig. 7(b), the frequency responses in the cases with stronger hardening spring nonlinearities show obvious differences from the classical lock-in where $f_y/f_n \approx 1$. Figs. 8 – 10 demonstrate the time history, PSD and phase-plane plots in different response regimes for $\lambda = -1.6, 0$ and 4, which respectively represent the softening spring, linear spring and hardening spring scenarios. In these figures, $t^* = tU_\infty/D$ is the dimensionless time and $d(y/D)/dt^*$ is the normalised vibration velocity. $Re = 80, 100, 160$ and 190 correspond to the initial, upper, lower and desynchronised branches in the softening and linear spring cases whereas for the hardening spring case, $Re = 80$, 90 and 170 are in the initial branch and $Re = 190$ and 210 belong to the upper branch and desynchronised region, respectively. The comparisons among the figures show that the response characteristics of the cylinder in the softening spring and linear spring cases are qualitatively similar. The

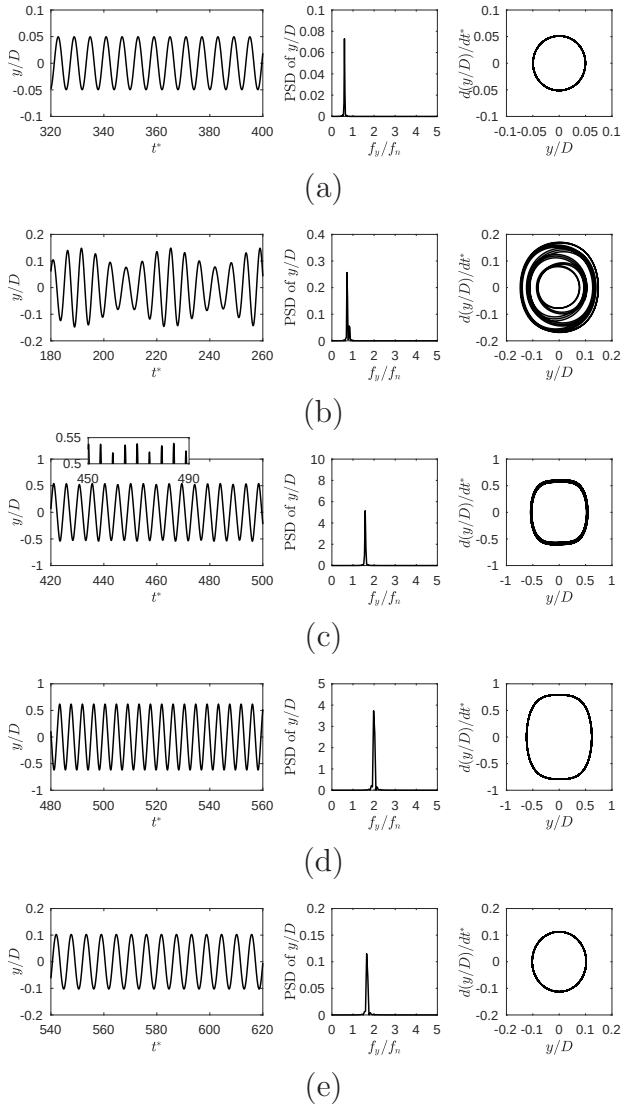

Fig. 10. Time history, power spectral density and phase-plane plots in different response regimes for $\lambda = 4$: (a) $Re = 80$, (b) $Re = 90$, (c) $Re = 170$, (d) $Re = 190$ and (e) $Re = 210$.

cylinder response in the four response regimes is featured by single-amplitude and single-period oscillations with highly repeatable phase-plane plots. As for the hardening spring case, the response of the cylinder is single-amplitude and single-period at the beginning of the initial branch when $Re = 80$. With an increase in Re to 90, an obvious beating phenomenon which is related to a mode change or a mode competition (Placzek et al., 2009) is observed. The PSD plot of y/D in Fig. 10(b) shows that the superposition of two close

frequencies contributes to the beating phenomenon. The beating response can be classified as quasi-periodic, which is confirmed by the doughnut-like phase plane (Modarres-Sadeghi et al., 2011) as illustrated by the phase-plane plot in Fig. 10(b). The beating response dies down as Re is gradually increased. It can be seen from the close-up view of the time history plot in Fig. 10(c) that when $Re = 170$ there are only some small fluctuations in the vibration amplitude from cycle to cycle in the range of $0.52D - 0.54D$. The PSD plot in Fig. 10(c) illustrates that the weaker frequency component near the primary oscillation frequency almost vanishes. The repeatability of the phase-plane plot is significantly improved with the overall curve being a bit thicker than that for the single-amplitude and single-frequency response. Similar to the softening and linear spring cases, the response of the cylinder regains its single-amplitude and single-frequency characteristics in the upper branch and the desynchronised regime.

4.3. Hydrodynamic coefficients

Figs. 11(a), (c) and (e) show the variation of the hydrodynamic force coefficients ($\overline{C}_D$, C'_D and C'_L) of a circular cylinder elastically supported by linear and softening springs with Re while Figs. 11(b), (d) and (f) are their counterparts for linear and hardening springs. According to the left column of Fig. 11, similar variation trends of the hydrodynamic force coefficients with Re are observed for the linear and softening springs. The shapes of the C'_D curves resemble those of the $\overline{C}_D$ curves. The peak values of $\overline{C}_D$ and C'_D for each individual λ appear at the same Re as the one corresponding to the maximum A_y/D. Both $\overline{C}_D$ and C'_D decrease as the nonlinearity of the softening spring grows stronger. The peak value of C'_L also decreases with decreasing λ. The maximum C'_L values for $\lambda = 0, -0.4, -0.8$ and -1.2 are all observed at $Re = 90$ while the Re corresponding to the maximum C'_L of $\lambda = -1.6$ shifts to a lower value of $Re = 80$.

Similar to the amplitude response envelope, when $\lambda \geq 0$, the hydrodynamic force coefficient envelopes move towards a higher Re range as λ is increased. The C'_D curves follow similar trends to those of $\overline{C}_D$. For a certain λ value, the maximum values of $\overline{C}_D$ and C'_D are also associated with the Re where the maximum A_y/D appears. The results of C'_L against Re for $\lambda \geq 0$ in Fig. 11(f) reflect that the maximum value of C'_L increases slightly as λ is increased.

The oscillation frequency of the cylinder can be described by the following equation (Dahl et al., 2010).

$$f_y = \sqrt{\frac{k}{m + m_{ea}}} \tag{7}$$

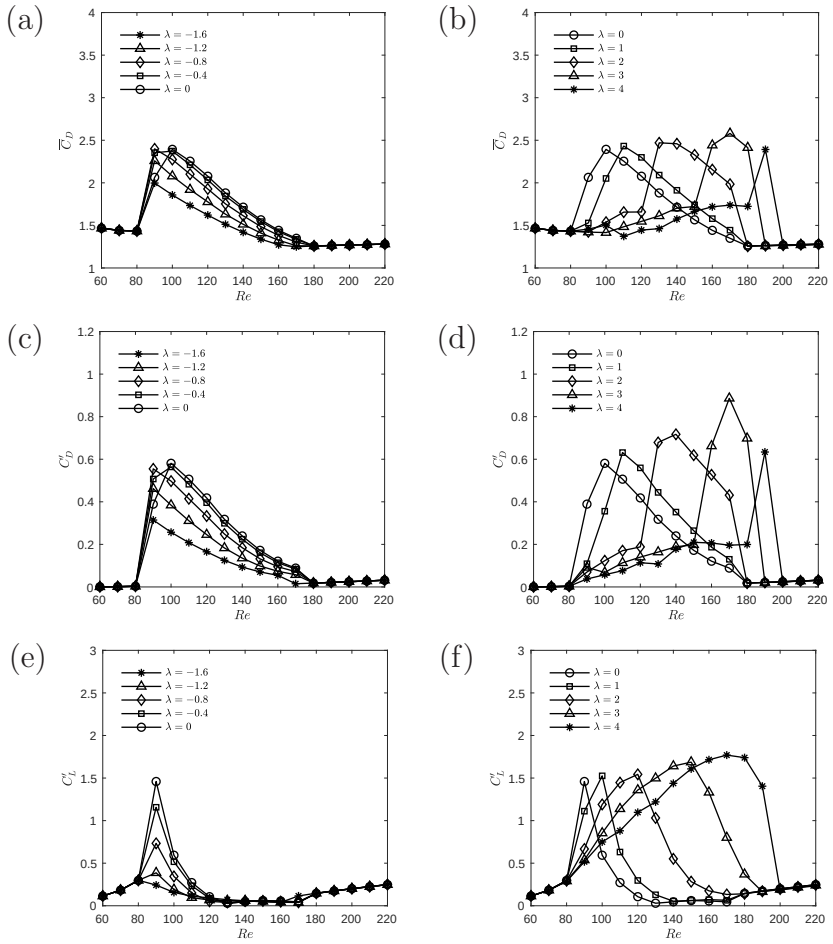

Fig. 11. Variation of the hydrodynamic force coefficients with the Reynolds number: (a) $\overline{C}_D$ for $\lambda \leq 0$, (b) $\overline{C}_D$ for $\lambda \geq 0$, (c) C'_D for $\lambda \leq 0$, (d) C'_D for $\lambda \geq 0$, (e) C'_L for $\lambda \leq 0$ and (f) C'_L for $\lambda \geq 0$.

where m_{ea} is the effective added mass which can be nondimensionalised in the same way as m^*, i.e., $C_m = 4m_{ea}/\rho\pi D^2$. C_m denotes the hydrodynamic coefficient due to the vortex dynamics which is in phase with the acceleration of the cylinder. According to Khalak and Williamson (1999) and Jauvtis and Williamson (2004), the effective added mass coefficient in the cross-flow direction (C_{my}) can be expressed as

$$C_{my} = \frac{2U_\infty^2 C_{L1}\cos(\phi_y)}{\pi(A_y/D)D^2(2\pi f_y)^2} \tag{8}$$

where C_{L1} and ϕ_y are the magnitude of the first harmonic component of C_L and its phase angle with respect to y/D, respectively.

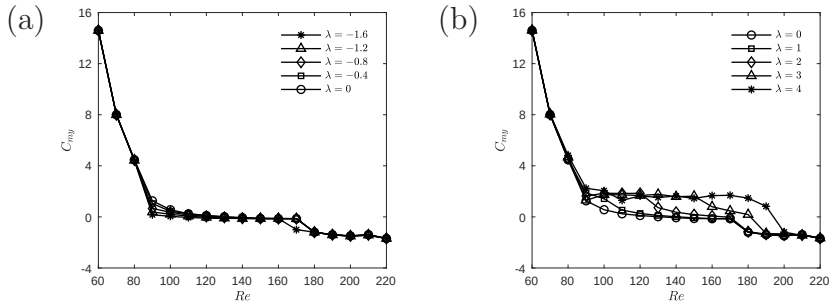

Fig. 12. Effective added mass coefficient as a function of the Reynolds number: (a) $\lambda \leq 0$ and (b) $\lambda \geq 0$.

As shown in Fig. 12(a), for $\lambda \leq 0$, C_{my} in the non-synchronous regions ($60 \leq Re \leq 80$ and $180 \leq Re \leq 220$) exhibits linearly decreasing trends with increasing Re, which causes the increases in f_y/f_n with Re in those regions. In the upper branch, C_{my} gradually approaches zero, while $C_{my} \approx 0$ in the lower branch. These observations correspond to the step change in f_y/f_n in the transition range from the upper branch to the lower branch and the synchronisation between f_y and f_n in the lower branch, respectively. Some discrepancies are observed in the C_{my} curves for different λ values in the initial-upper branch transition as a result of the variation of the softening spring nonlinearity. When $Re = 170$, C_{my} of $\lambda = -1.6$ is evidently lower than those for the other four λ values in Fig. 12(a), which is reflected by the earlier transition from the lower branch to the desynchronised region in the highly nonlinear softening spring case.

Fig. 12(b) illustrates the variation of C_{my} with Re when $\lambda \geq 0$. It can be seen from the figure that the C_{my} curve of a moderate λ value ($\lambda = 1$) coincides with that of the linear system except for some small discrepancies in the transition region from the initial branch to the upper branch, which leads to the similar frequency responses between $\lambda = 0$ and 1. With the increase in λ, larger deviation in the C_{my} curve is observed and the C_{my} value is no longer around 0, which leads to the nonlinear variation of f_y/f_n with Re in the hardening spring cases with stronger nonlinearities as discussed in Section 4.2.

4.4. Effect of cubic stiffness nonlinearity

As the standard definition of V_r is no longer valid in the cubic spring cases, all the results presented in the previous sections are scaled with Re. In this section, we will try to explain the nonlinear VIV results by applying the knowledge of a standard linear VIV system. In order to achieve this goal,

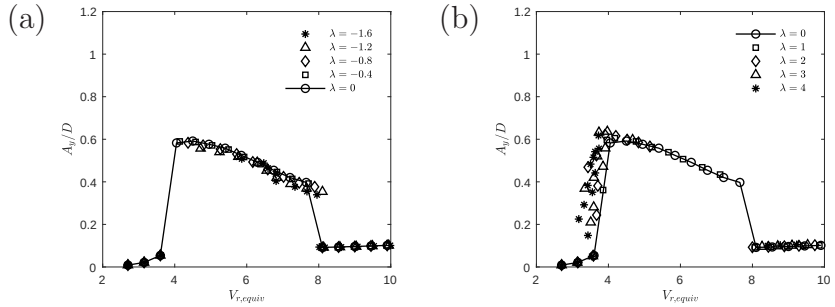

Fig. 13. Response amplitude against the equivalent reduced velocity: (a $\lambda \leq 0$ and (b) $\lambda \geq 0$.

the response data need to be plotted against a nondimensional variable similar to V_r. As is known, the natural frequency of a cubic spring depends on the vibration amplitude. Therefore, it cannot be determined a priori but can be calculated after the vibration amplitudes are obtained. Here, the unforced Duffing oscillator equation is numerically solved using a fourth-order Runge-Kutta method with an adaptive time-step size to derive the natural frequency of a cubic spring at each vibration amplitude ($f_n(A_y/D)$). Then, the equivalent reduced velocity proposed by Mackowski and Williamson (2013) which can be defined as

$$V_{r,equiv} = \frac{U_\infty}{f_n(A_y/D)D} \tag{9}$$

is used to make sense of the nonlinear VIV data. Fig. 13 shows the variation of A_y/D with $V_{r,equiv}$ for linear and cubic springs. It is observed that the results of the cubic spring collapse very well with those of the linear system, which suggests that it is possible to extrapolate the nonlinear VIV results from the linear VIV data. The reason why this good collapse can be achieved using $V_{r,equiv}$ is that as a matter of fact, a nonlinear spring can alter the linear relationship between V_r and Re in the linear VIV system. $V_{r,equiv}$ is plotted as a function of Re for the linear and cubic springs in Fig. 14. As shown in the figure, the $V_{r,equiv}$ curves of $\lambda = 0$ and -0.4 nearly collapse into a single linear curve corresponding to the similar amplitude responses for these two λ values as shown in Fig. 4(a). As λ is decreased, nonlinear changes of $V_{r,equiv}$ with Re start to occur in the range of $Re = 90 - 170$. Stronger softening spring nonlinearity results in more evident nonlinear variation of $V_{r,equiv}$ with Re. Similar to the softening spring cases, for $\lambda \geq 0$, the cubic stiffness nonlinerity breaks the fixed proportionate relationship between V_r and Re in the linear spring case within a certain Re range and changes the natural frequency of the cubic spring with the vibration amplitude. These conclusions agree with those drawn by Mackowski and Williamson (2013) in their experimental

tests in a subcritical Re range. Such features are very useful in engineering applications. On the one hand, an appropriate cubic spring can help a VIV energy harnessing device maintain its optimal power conversion over a wider range of the flow velocities and on the other hand, by introducing a certain amount of cubic stiffness nonlinearity, the V_r values prone to VIV can be transited quickly with increasing flow velocity to avoid excessive vibrations.

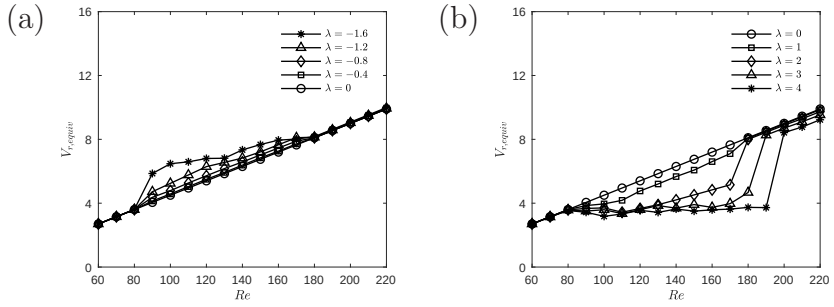

Fig. 14. Equivalent reduced velocity versus the Reynolds number: (a) $\lambda \leq 0$ and (b) $\lambda \geq 0$.

4.5. Vortex shedding patterns

In this section, the nondimensional spanwise vorticity contours are used to evaluate the flow patterns associated with the oscillating cylinder. The nondimensional vorticity in the spanwise direction is defined as $\omega_z = (\partial v/\partial x - \partial u/\partial y)/(U_\infty/D)$. Fig. 15 shows the spanwise vorticity contours at different Re for $\lambda = -1.6, 0$ and 4. The three λ values represent the softening, linear and hardening spring cases, respectively and Re ranges from 70 to 210 with an increment of 20 which covers the different response regimes. As shown in Fig. 15(a), in the highly nonlinear softening spring case, the wake behind the cylinder demonstrates a single-row configuration which resembles the classical Kármán vortex street in all the four response branches. In terms of the linear spring case when $\lambda = 0$, a single-row vortex street is observed in the initial branch when A_y/D of the cylinder is small. With the increase in the flow velocity approaching the upper branch, the vortex shedding exhibits a double-row configuration. The double-row vortex street is more consistent at $Re = 90$ because of the larger vibration amplitude. A slight decrease in the vibration amplitude leads to the formation of the double-row configuration being delay to a downstream location when $Re = 110$. A further increase in the flow velocity causes an ulterior reduction in the vibration amplitude to around $0.52D$ at $Re = 130$ and the wake behind the cylinder narrows to a single-row configuration. This verifies that the observation of a single-row

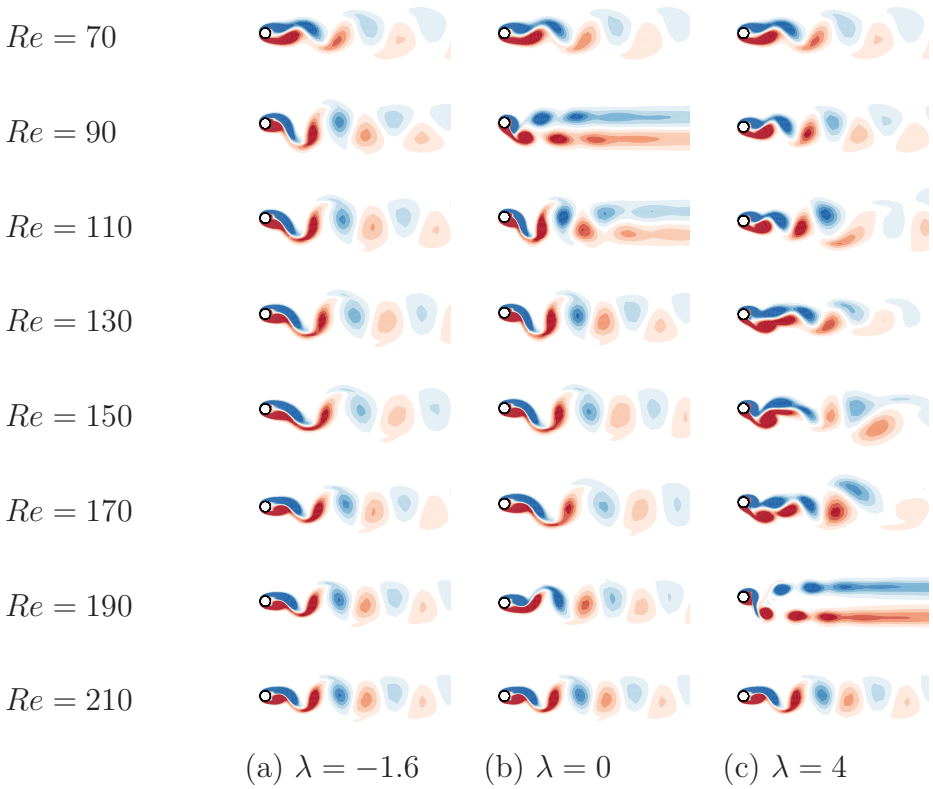

Fig. 15. Spanwise vorticity contours at different Reynolds numbers: (a) $\lambda = -1.6$, (b) $\lambda = 0$ and (c) $\lambda = 4$.

vortex street in the four response regimes for the highly nonlinear softening spring case with $\lambda = -1.6$ is attributed to the fact that the vibration amplitude in that case is always smaller than $0.51D$. As the response of the cylinder transits through the lower branch and the desynchronised region, the width of the cylinder wake reduces with decreasing A_y/D. When λ is increased to 4, in the initial branch, a single-row vortex street is persisted up to $Re = 110$ although the beating phenomenon first appears at $Re = 90$. With the increase in Re, the growth in A_y/D together with the gradually diminishing beating response contributes to the disorders in the wake. The evolutions of the wake over time for the different cases in which the beating phenomenon is observed in the hardening spring case of the present study will be discussed later. Similar to the linear spring case, on reaching the upper branch at $Re = 190$, the vortex shedding pattern exhibits a double-row vortex street. Further increasing Re to the desynchronised region, the significant decrease in A_y/D regulates the vortex street to a single row.

Leontini et al. (2006) found in their study that the wake associated with

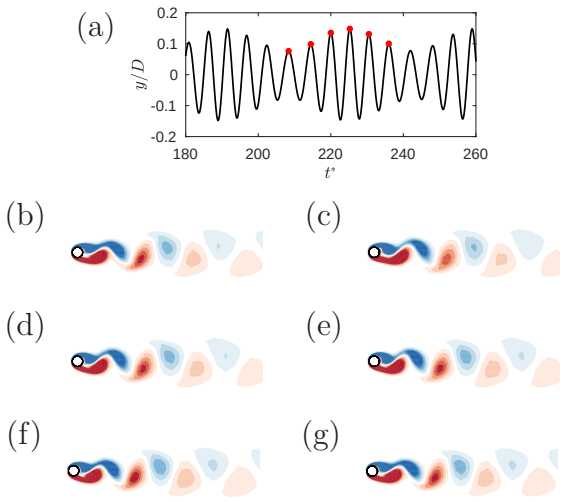

Fig. 16. Time history of the displacement and the spanwise vorticity contours at different time instants for $Re = 90$ when $\lambda = 4$: (a) displacement time history, (b) $t^* = 208.38$, (c) $t^* = 214.49$, (d) $t^* = 220.01$, (e) $t^* = 225.25$, (f) $t^* = 230.5$ and (g) $t^* = 235.99$.

the beating response varied with time from order to disorder then back to order again. In order to examine whether their finding is also applicable to the beating phenomenon observed in the hardening spring case of the present study, the spanwise vorticity contours at different time instants for $Re = 90$

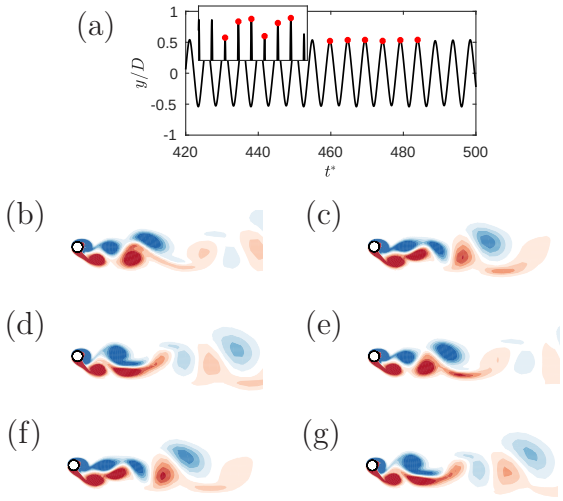

Fig. 17. Time history of the displacement and the spanwise vorticity contours at different time instants for $Re = 170$ when $\lambda = 4$: (a) displacement time history, (b) $t^* = 459.78$, (c) $t^* = 464.66$, (d) $t^* = 469.43$, (e) $t^* = 474.29$, (f) $t^* = 479.17$ and (g) $t^* = 483.94$.

and 170 of the hardening spring case are analysed. Thereinto, $Re = 90$ at $\lambda = 4$ stands for the case close to the low end of the initial branch where the beating phenomenon is first observed and the modulations in the vibration amplitude from cycle to cycle is evident. The vorticity contours at six different time instants denoted by the red dots in Fig. 16(a) are provided in the chronological order from Fig. 16(b) to Fig. 16(g). As shown in Figs. 16(b) – (g), the vortex shedding patterns at the six time instants are very much alike regardless of the modulations in the vibration amplitude in the different cycles. The reason for the similar wake flow fields corresponding to the beating phenomenon at $Re = 90$ and $\lambda = 4$ is that the beating response takes place near the beginning of the initial branch where the displacement amplitude is small. The interaction and coupling between the phase of vortex shedding and the fluctuating oscillation amplitude are not very strong. Fig. 17 presents the time history of the displacement and the spanwise vorticity contours at different time instants for $Re = 170$ when $\lambda = 4$. This denotes the case in which the beating phenomenon is fading away before the single-amplitude and single-period oscillations dominating the cylinder response again. The spanwise vorticity contours represent six time instants in two growth-decay cycles as depicted by the red dots in Fig. 17(a). It can be observed from Fig. 17(b) that when the cylinder is vibrating at a smaller amplitude, the vortex shedding pattern is regular with a very narrow double-row configuration in the near wake convecting into a single row in the far wake. Under the effect of resonance, the oscillation grows over time and coalescence of the same-sign vortices are observed causing the wake to become disordered as demonstrated in Figs. 17(c) and (d). As mentioned by Leontini et al. (2006), the disordering of the wake induces a drop in the lift force which leads to a reduction in the oscillation amplitude. With the reduction in the vibration amplitude, the wake regains its regularity and the growth-decay cycle commences again (see Figs. 17(e) – (g)). This mechanism is similar to the one argued by Leontini et al. (2006). However, the difference is that the disordering of the wake is not as strong as that in their case because of the weaker amplitude modulations in the vibration response of the present case. Consequently, the reduction in lift and the subsequent decrease in the vibration amplitude are weaker. Therefore, the modulations in the oscillation amplitude in the present case are not as strong.

It is found that all the vortex shedding patterns in the present study are in the 2S mode with the absence of the 2P wake mode associated with the upper and lower branches in the higher Re experiments, which indicates that at low Re, the transition of the response regime need not to be accompanied by a change in the vortex shedding mode. This conclusion agrees with that in Bao et al. (2011). However, it should be noted that the 2S wake flow patterns in

the upper and lower branches of the present simulations share similar features to the 2P vortex shedding modes in the corresponding response branches in the higher Re experiments. As discussed by Leontini et al. (2006), the 2P and 2S vortex shedding modes both consist of a half-period evolution and a spatial reflection about the wake centreline except that the vortical structures of the 2S mode do not split in the near wake like the 2P mode in Govardhan and Williamson (2000). The difference in the vortex shedding patterns in the upper and lower response branches could possibly be attributed to the effect of Re.

5. Conclusions

2D FSI simulations are performed to quantify the effect of the cubic stiffness nonlinearity on the 1DOF cross-flow VIV of an elastically mounted circular cylinder in a Re range of 60 – 220. A low mass ratio of $m^* = 2.546$ and zero structural damping are considered in the simulations. The dimensionless cubic stiffness nonlinearity strength (λ) is varied from -1.6 to 4. The numerical results are analysed in detail and the conclusions of the present study are as follows.

When $\lambda \leq 0$, four distinct response regimes (i.e., the initial, upper, lower and desynchronised branches) analogous to those in the higher Re experiments are observed. In the low Re range considered in the present study, the overall VIV response of the cylinder at $\lambda = -0.4$ generally agrees with that of the linear system. As the softening spring nonlinearity grows stronger, the maximum attainable amplitude decreases and the Re corresponding to the maximum A_y/D shifts to a lower value. The synchronous regions with larger vibration amplitude for $-1.2 \leq \lambda \leq 0$ are identical in the range of $Re = 90 - 170$. When λ is decreased to -1.6, the lock-in range becomes narrower and the cylinder response transits to the desynchronised region at $Re = 160$. The initial-upper branch and the upper-lower branch transition regions, to some extent, move towards lower Re ranges. With regard to the hardening spring, as λ is increased, the VIV response envelope shifts to a higher Re range with a smoother variation of the amplitude response in the initial and upper branches and a gradually vanishing lower branch of response. Although the hardening spring has a significant effect on the amplitude response profile, its influence on the maximum attainable amplitude is non-distinctive.

Similar frequency responses are observed for $\lambda = 0, -0.4$ and -0.8. the dimensionless oscillation frequency (f_y/f_n) coincides with the Strouhal frequency in the Re range of 60 – 80. In the synchronous region, f_y/f_n undergoes a step change and approaches $f_y/f_n = 1$ in the transition region

between the upper and lower branches. In the desynchronised region, f_y/f_n varies linearly with Re. As the softening spring nonlinearity grows stronger, the frequency response in the initial excitation and desynchronised regions are similar to those of the linear and weaker softening springs. Discrepancies mainly appear in the lock-in range and f_y/f_n of the stronger softening spring is lower than $f_y/f_n = 1$ in the linear and weaker softening spring cases. When $\lambda > 0$, the frequency response shows good agreement with that of the linear system in the initial excitation and desynchronised regions. The variation trend of the frequency response at $\lambda = 1$ is qualitatively similar to the linear spring one with f_y/f_n in the larger-amplitude range being slightly higher than $f_y/f_n = 1$. As λ is increased, f_y/f_n varies nonlinearly with Re. In the hardening spring case, a quasi-periodic beating response is observed near the start of the initial branch and the modulations in the vibration amplitude in different cycles reduce as Re is increased. The cylinder response turns back to single-amplitude and single-period in the upper branch and desynchronised regime.

The hydrodynamic force coefficient envelopes move along the Re axis when λ is varied. In general, the root mean square drag coefficient (C'_D) and the mean drag coefficient ($\overline{C}_D$) curves share similar variation trends with Re. The maximum values of $\overline{C}_D$ and C'_D usually appear at the Re corresponding to the maximum vibration amplitude. In the softening spring case, the maximum values of $\overline{C}_D, C'_D$ and the root mean square lift coefficient (C'_L) all decrease with decreasing λ. Whereas, a slight increase in the maximum value of C'_L as λ is increased is observed for the hardening spring case. When $\lambda \leq 0$, the cross-flow added mass coefficient (C_{my}) decreases linearly with the increase in Re in the non-synchronous regions. The C_{my} curves exhibit some discrepancies in the transition region between the initial and upper branches at different λ values. As for $\lambda \geq 0$, the variation of C_{my} with Re at $\lambda = 1$ almost agrees with that for the linear system. The increase in λ leads to the departure of the C_{my} curve from the linear one.

The nonlinear VIV results collapse well with the linear VIV data when they are presented with respect to the equivalent reduced velocity ($V_{r,equiv}$) indicating the feasibility of predicting the response of a cubic-spring system by using the response data of a linear system. The cubic stiffness nonlinearity essentially breaks the fixed proportionate relationship between V_r and Re in the linear system and varies $V_{r,equiv}$ nonlinearly with Re. This feature is extremely important as it suggests that the cubic stiffness nonlinearity could be utilised either to enhance the V_r range in which the large-amplitude vibrations occur so that a device harnessing energy from VIV could make better use of those vibrations or to reduce that range to protect the structural components from catastrophic failures.

The vortex shedding in the highly nonlinear softening spring case shows a single-row configuration which resembles the classical Kármán vortex street. For the linear VIV system, a single-row vortex street is observed for the initial, lower and desynchronised branches. When the cylinder response is in the upper branch, the vortex street in the wake of the cylinder widens and exhibits a double-row configuration. In terms of the highly nonlinear hardening spring case, the wake flow field shows a single-row configuration at the beginning of the initial branch as well as in the desynchronised region. A regular single-row vortex street is also observed in the cases near the low end of the initial branch where there exists the beating phenomenon in the cylinder response. With the increase in Re and A_y/D, disorders in the wake are found to be associated with the gradually weakening beating response of the cylinder. The vortices behind the cylinder arrange themselves into a double-row vortex street in the upper branch of the highly nonlinear hardening spring case. Because of the low Re range considered in the present simulations, only the 2S vortex shedding mode is identified.

Overall, the amplitude response features of the 1DOF VIV of a circular cylinder elastically supported by a cubic spring in the present research are comparable with the previous experimental results at higher Re, while the present study supplement the existing literature with other important aspects of the nonlinear VIV such as the frequency response, the hydrodynamic coefficients and the vortex shedding modes. The numerical results provide detailed information about the nonlinear VIV response characteristics and also shed light on the mechanism of how the cubic stiffness nonlinearity affects the VIV of a circular cylinder. In the present study, only the cubic stiffness nonlinearity is considered at low Re and a fixed zero damping. More systematic investigations on the effects of different forms of nonlinear restoring forces and different damping ratios in a higher Re range will be performed in the future.

Acknowledgements

This research work was financially supported by National Natural Science Foundation of China (Grant Number: 51679167), the Science Fund for Creative Research Groups of the National Natural Science Foundation of China (Grant Number: 51621092) and China Postdoctoral Science Foundation (Grant Number: 2018M641652).

References

Ahn, H. T., Kallinderis, Y., 2006. Strongly coupled flow/structure interactions with a geometrically conservative ALE scheme on general hybrid

meshes. Journal of Computational Physics 219, 671–696.

Bao, Y., Huang, C., Zhou, D., Tu, J., Han, Z., 2012. Two-degree-of-freedom flow-induced vibrations on isolated and tandem cylinders with varying natural frequency ratios. Journal of Fluids and Structures 35, 50–75.

Bao, Y., Zhou, D., Tu, J., 2011. Flow interference between a stationary cylinder and an elastically mounted cylinder arranged in proximity. Journal of Fluids and Structures 27, 1425–1446.

Barton, D. A. W., Burrow, S. G., Clare, L. R., 2010. Energy harvesting from vibrations with a nonlinear oscillator. Journal of Vibration and Acoustics 132, 021009.

Bearman, P. W., 1984. Vortex shedding from oscillating bluff bodies. Annual Review of Fluid Mechanics 16, 195–222.

Bearman, P. W., 2011. Circular cylinder wakes and vortex-induced vibrations. Journal of Fluids and Structures 27, 648–658.

Bert, C. W., Egle, D. M., Wilkins, Jr., D. J., 1990. Optimal design of a nonlinear dynamic absorber. Journal of Sound and Vibration 137, 347–352.

Blackburn, H., Henderson, R., 1996. Lock-in behavior in simulated vortex-induced vibration. Experimental Thermal and Fluid Science 12, 184–189.

Blevins, R. D., 1986. Flow-Induced Vibration. Robert E. Krieger Publishing Company, Inc., Florida, USA.

Bloor, M. S., 1964. The transition to turbulence in the wake of a circular cylinder. Journal of Fluid Mechanics 19, 290–304.

Borazjani, I., Sotiropoulos, F., 2009. Vortex-induced vibrations of two cylinders in tandem arrangement in proximity-wake interference region. Journal of Fluid Mechanics 621, 321–364.

Bourguet, R., Karniadakis, G. E., Triantafyllou, M. S., 2011. Lock-in of the vortex-induced vibrations of a long tensioned beam in shear flow. Journal of Fluids and Structures 27, 838–847.

Brika, D., Laneville, A., 1993. Vortex-induced vibrations of a long flexible circular cylinder. Journal of Fluid Mechanics 250, 481–508.

Dahl, J. M., Hover, F. S., Triantafyllou, M. S., Oakley, O. H., 2010. Dual resonance in vortex-induced vibrations at subcritical and supercritical Reynolds numbers. Journal of Fluid Mechanics 643, 395–424.

Feng, C. C., 1968. The measurements of vortex-induced effects in flow past stationary and oscillating circular and D-section cylinders. Master's thesis, University of British Columbia, Vancouver, Canada.

Gabbai, R. D., Benaroya, H., 2005. An overview of modelling and experiments of vortex-induced vibrations of circular cylinders. Journal of Sound and Vibration 282, 575–646.

Gammaitoni, L., Neri, I., Vocca, H., 2009. Nonlinear oscillators for vibration energy harvesting. Applied Physics Letters 94, 164102.

Gendelman, O. V., Vakakis, A. F., Bergman, L. A., McFarland, D. M., 2010. Asymptotic analysis of passive nonlinear suppression of aeroelastic instabilities of a rigid wing in subsonic flow. SIAM Journal on Applied Mathematics 70, 1655–1677.

Govardhan, R., Williamson, C. H. K., 2000. Modes of vortex formation and frequency response of a freely vibrating cylinder. Journal of Fluid Mechanics 420, 85–130.

Guilmineau, E., Queutey, P., 2004. Numerical simulation of vortex-induced vibration of a circular cylinder with low mass-damping in a turbulent flow. Journal of Fluids and Structures 19, 449–466.

Issa, R. I., 1986. Solution of the implicitly discretised fluid flow equations by operator-splitting. Journal of Computational Physics 62, 40–65.

Jauvtis, N., Williamson, C. H. K., 2004. The effect of two degrees of freedom on vortex-induced vibration at low mass and damping. Journal of Fluid Mechanics 509, 23–62.

Khalak, A., Williamson, C. H. K., 1997. Fluid forces and dynamics of a hydroelastic structure with very low mass and damping. Journal of Fluids and Structures 11, 973–982.

Khalak, A., Williamson, C. H. K., 1999. Motions, forces and mode transitions in vortex-induced vibrations at low mass-damping. Journal of Fluids and Structures 13, 813–581.

Lee, Y. S., Vakakis, A. F., Bergman, L. A., McFarland, D. M., Kerschen, G., Nucera, F., Tsakirtzis, S., Panagopoulos, N., 2008. Passive nonlinear targeted energy transfer and its applications to vibration and absorption: A review. Proceedings of the Institution of Mechanical Engineers Part K Journal of Multi-body Dynamics 222, 77–134.

Leontini, J. S., Thompson, M., Hourigan, K., 2007. Three-dimensional transition in the wake of a transversely oscillating cylinder. Journal of Fluid Mechanics 577, 79–104.

Leontini, J. S., Thompson, M. C., Hourigan, K., 2006. The beginning of branching behaviour of vortex-induced vibration during two-dimensional flow. Journal of Fluids and Structures 22, 857–864.

Ma, C., Sun, H., Nowakowski, G., Mauer, E., Bernitsas, M. M., 2016. Nonlinear piecewise restoring force in hydrokinetic power conversion using flow induced motions of a single cylinder. Ocean Engineering 128, 1–12.

Mackowski, A. W., Williamson, C. H. K., 2013. An experimental investigation of vortex-induced vibration with nonlinear restoring forces. Physics of Fluids 25, 087101.

Modarres-Sadeghi, Y., Chasparis, F., Tirantafyllou, M. S., Tognarreli, M., Beynet, P., 2011. Chaotic response is a generic feature of vortex-induced vibrations of flexible risers. Journal of Sound and Vibration 330, 2565–2579.

Newmark, N. M., 1959. A method of computation for structural dynamics. Journal of Engineering Mechanics 85, 67–94.

OpenFOAM, 2015. OpenFOAM v3 User Guide. The OpenFOAM Foundation.

Païdoussis, M. P., Price, S. J., de Langre, E., 2014. Fluid-Structure Interactions: Cross-Flow-Induced Instabilities. Cambridge University Press, New York, USA.

Pan, Z., Cui, W., Miao, Q., 2007. Numerical simulation of vortex-induced vibration of a circular cylinder at low mass-damping using RANS code. Journal of Fluids and Structures 23, 23–37.

Placzek, A., Sigrist, J., Hamdouni, A., 2009. Numerical simulation of an oscillating cylinder in a cross-flow at low Reynolds number: Forced and free oscillations. Computers and Fluids 38, 80–100.

Ramesh, K., Murua, J., Gopalarathnam, A., 2015. Limit-cycle oscillations in unsteady flows dominated by intermittent leading-edge vortex shedding. Journal of Fluids and Structures 55, 84–105.

Stappenbelt, B., 2010. The effect of non-linear mooring stiffness on the vortex-induced motion of cylindrical structures. In: Proceedings of the Twentieth (2010) International Offshore and Polar Engineering Conference. Beijing, China.

Sumer, B. M., Fredsøe, J., 2006. Hydrodynamics Around Cylindrical Structures. World Scientific Publishing Co. Pte. Ltd., London, UK.

Sun, H., Ma, C., Bernitsas, M. M., 2018. Hydrokinetic power conversion using flow induced vibrations with cubic restoring force. Energy 153, 490–508.

Wang, E., Ramesh, K., Killen, S., Viola, I., 2018. On the nonlinear dynamics of self-sustained limit-cycle oscillations in a flapping-foil energy harvester. Journal of Fluids and Structures 83, 339–357.

Wang, E., Xiao, Q., 2016. Numerical simulation of vortex-induced vibration of a vertical riser in uniform and linearly sheared currents. Ocean Engineering 121, 492–585.

Wang, E., Xiao, Q., Incecik, A., 2017. Three-dimensional numerical simulation of two-degree-of-freedom VIV of a circular cylinder with varying natural frequency ratios at $Re = 500$. Journal of Fluids and Structures 73, 162–182.

Williamson, C. H. K., 1988. The existence of two stages in the transition to three-dimensionality of a cylinder wake. Physics of Fluids 31, 3165–3168.

Williamson, C. H. K., Govardhan, R., 2004. Vortex-induced vibrations. Annual Review of Fluid Mechanics 36, 413–455.

Zhao, M., 2013. Flow induced vibration of two rigidly coupled circular cylinders in tandem and side-by-side arrangements at a low Reynolds number of 150. Physics of Fluids 25, 123601.

Zhao, M., 2015. Numerical simulation of vortex-induced vibration of a circular cylinder in a spanwise shear flow. Physics of Fluids 27, 063101.

Zhao, M., Cheng, L., An, H., Lu, L., 2014. Three-dimensional numerical simulation of vortex-induced vibration of an elastically mounted rigid circular cylinder in steady current. Journal of Fluids and Structures 50, 292–311.